Cement and Concrete Composites 120 (2021) 104037

Contents lists available at ScienceDirect

Cement and Concrete Composites

journal homepage: http://www.elsevier.com/locate/cemconcomp

3D printing eco-friendly concrete containing under-utilised and waste solids as aggregates

Gang Bai [a], Li Wang [a,*], Guowei Ma [a,b], Jay Sanjayan [c], Mingke Bai [d]

[a] School of Civil and Transportation Engineering, Hebei University of Technology, 5340 Xiping Road, Beichen District, Tianjin, 300401, China
[b] Tianjin Key Laboratory of Prefabricated Building and Intelligent Construction, Hebei University of Technology, 5340 Xiping Road, Beichen District, Tianjin, 300401, China
[c] Faculty of Science, Engineering and Technology, Swinburne University of Technology, Victoria, 3122, Australia
[d] Yaobai Special Cement Technology R & D Co., Ltd., 336 Shenzhou 4th Road, Chang'an District, Xi'an, 710100, China

ARTICLE INFO

Keywords:
3D printing concrete
Re-utilisation of solid resource
Particle grading
Printability
Interlayer bonding
Shrinkage

ABSTRACT

3D concrete printing is an emerging construction technology, and presents an opportunity for utilising materials that are otherwise considered unsuitable for concrete construction. Incorporating underutilised solids and/or waste solids as aggregates is a way of gaining the maximum environmental and economic benefits from the emerging 3D concrete printing technology. In this study, desert sand (small size), river-sediment ceramsite sand (medium size), and recycled concrete (large size) were experimentally investigated for use as aggregates in the 3D printing of concrete. Three mixtures were designed with continuous, open, and interrupted gradations of solids, respectively, based on the theory of particle interference, and aiming to meet the requirements of extrusion-based 3D printing. The influences of the particle grading characteristics on the printability-related early-age behaviours, mechanical properties, and shrinkage resistance have been measured and analysed. The test results demonstrate that the self-supporting skeletal effect formed by the gradated particles reduces the flowability of the mixtures, but the structural build-up/buildability performance is improved (under the premise of the desired printability). The interlayer distribution and skeleton of the gradated aggregate contribute to improving the interfacial interlocking effect and contact bonding between layers; this is visually validated through computed tomography (CT) scanning. Further, the addition of aggregates reduces the proportion of cementitious composites, and therefore effectively mitigates the shrinkage of the cement matrix. The grading characteristics of the underutilised particle resources are crucial for regulating the early-age 3D printability. This article provides feasible solutions based on experimental data for promoting the eco-utilisation of underutilised and waste solids in 3D printing, and these solutions satisfy the minimum strength and durability requirements.

1. Introduction

3D concrete printing (3DCP), an emerging digital fabrication technology using concrete, promises to deliver greater automation, flexibility, and freeform construction as compared to conventional (largely manual) construction. 3DCP can potentially assist in the integration of digital technologies such as building information modelling and virtual reality with construction [1–6]. In recent years, 3DCP has been successfully used for the construction of infrastructures, such as for pedestrian bridges, bus stations, and landscape architectures, as shown in Fig. 1. Thus, it demonstrates great potential and prospects for construction applications.

The major hurdles remaining for researchers in 3DCP include the weak interface bonding and mesoscale flaws between adjacent filaments, inadequate automated reinforcement methods, and lack of design, manufacturing, and quality evaluation specifications/standards for the printed materials and structures. Until these issues are satisfactorily resolved, 3DCP will not replace or change traditional construction methods. Currently, 3DCP is being used in the construction of special-shaped structures and in low-risk structures where the strength and durability requirements are minimised, as a way of exploring real-life applications.

As 3DCP is a new technology, it presents an opportunity to use more eco-friendly materials than those used in traditional construction. Most studies so far have focused on the printability and sustainability of eco-friendly cementitious systems such as alkali-activated mortars [10–12],

* Corresponding author.
E-mail address: wangl1@hebut.edu.cn (L. Wang).

https://doi.org/10.1016/j.cemconcomp.2021.104037
Received 6 October 2020; Received in revised form 18 February 2021; Accepted 26 March 2021
Available online 31 March 2021

as conventional cement is responsible for high levels of global carbon emissions. In conventional concrete, the aggregate forms more than half the amount of the concrete materials. There is a common preference for virgin aggregates, as it is more convenient to control the quality of the supply; however, this approach is increasingly becoming a major burden on natural resources. Therefore, many studies have attempted to use alternative aggregates to formulate 3D printable cementitious materials. For instance, Ma et al. [13] prepared 3D printing composites by incorporating copper tailings, and proposed extrudability and buildability coefficients for evaluating the printable properties. Xiao et al. [14–16] studied the possibility of using recycled sand/aggregate instead of natural sand/aggregate to develop 3D printing concrete; the applicability of the 3D printing recycled sand composites was validated based on the on-site printing of a room.

The manufacturing of 3D printing concrete usually incorporates a high content of non-renewable resources, including river sand, silica sand, and natural aggregate [17,18]. The exploration of eco-friendly solutions for replacing the natural (fine) aggregates by the proper adoption of underutilised and waste solids is important for addressing the shortages of natural resources and serious deterioration of the ecological environment induced by the improper treatment and low recycling rates of solid waste resources [19,20]. Desert sand (DS), ceramsite particles (CPs), and recycled concrete aggregate (RA) are three different types of underutilised or waste solids that have been adopted in concrete as aggregates of small, medium, and large sizes, respectively [21–23].

***DS*:** According to statistics, desert areas account for approximately 33% of the total land area. DS could serve as an abundant alternative sand resource for preparing concrete. The grain size of DS is usually between 0.08 and 0.40 mm. It is widely used for optimising the particle size distribution in concrete, improving the working performance, enhancing the material compactness, improving the compressive strength and toughness, effectively eliminating the freeze-thaw damage in concrete, and reducing the cost [24–26].

CPs: The manufacturing of ceramsite is an effective approach to managing river sediment and lake silt. Adopting CPs as building materials provides lightweight thermal insulation, and relieves the negative impact of the silt on the ecological environment [27]. CPs are a type of closed fine-honeycomb microporous structure material wrapped by a hard ceramic shell, and provide light porosity, heat preservation, heat insulation, salt resistance, and freezing acid resistance. They have become the main raw materials for the preparation of lightweight concrete [28].

RA: The construction and demolition waste generated each year accounts for half of urban solid waste; this threatens the urban environment, as less than 5% of this waste is recycled and reused, and most of it is landfilled. The research on and applications of RA concrete are relatively mature. For example, it is widely used in the manufacturing of floor tiles [29], preparation of self-compacting concrete [30], production of structural components [31] and pavement construction [32].

The utilisation of desert sand, ceramsite particles, and recycled concrete as aggregates for optimising the composition of 3DCP raw materials and expanding the range of aggregate particle sizes is consistent with the aims of 3DCP technology, i.e. to provide economic and environmental benefits [14]. However, so far, there has been very little research in this area.

Previous studies using fine aggregate mortars have proven that the continuous grading (CG) of fine aggregates contributes to achieving the optimal static and dynamic yield stress and lowest plastic viscosity in cementitious materials. These are important for improving the printability and buildability performances [33–36]. The incorporation of alternative aggregates in the concrete for 3DCP poses technical difficulties in regard to providing smooth extrusion (extrudability) and stable deposition (buildability). This is particularly the case for waste solids. The effects of the sizes and particle gradations of the coarse aggregates on the printability and mechanical behaviours of the concrete require further analysis and investigation.

This study investigates of alternative aggregates composed of DS, CPs, and RA, as formulated with three types of gradings: continuous dense grading (CG), continuous open grading (OG), and interruption/discontinuous dense grading (IG). The effects on fresh concrete properties such as flowability, buildability, and printability, as well as on hardened concrete properties such as the mechanical and shrinkage properties, are reported and discussed. The meso-structure of the concrete is probed through advanced computed tomography (CT) scanning. A methodology is presented for the optimisation of the 3D printing concrete.

2. Materials and methods

2.1. Physical characterization of particles

The raw materials used in the manufacturing of printing concrete are DS, river-sediment CPs, and recycled concrete as the RA. Their geometrical morphologies are illustrated in Fig. 2. The mud content of these three aggregates was processed and controlled to be less than

Fig. 1. 3D printed concrete bridges (a) constructed in the Netherlands with a span of 12.0 m [7], (b) built at the campus of Hebei University of Technology (China) with a span of 17.94 m [8], and (c) 3D-printed bus station [9].

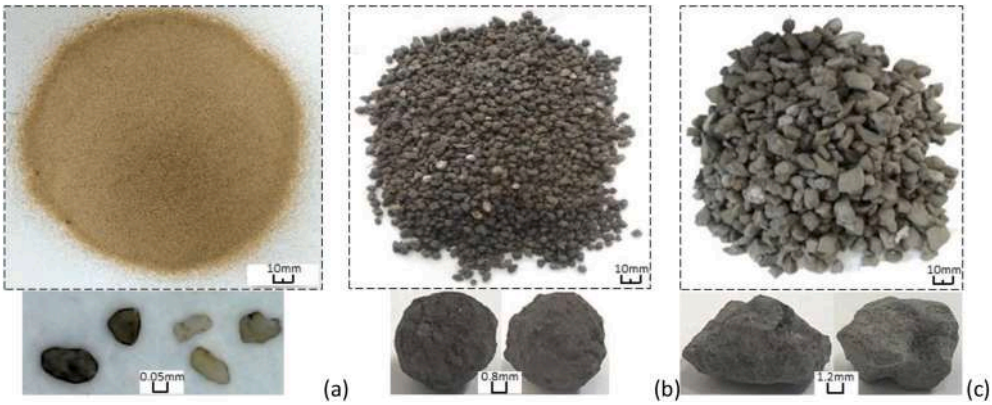

Fig. 2. Solid waste aggregate (a) desert sand (b) ceramsite particles (c) recycled aggregate.

0.4%. The size distribution characteristics of each aggregate are shown in Fig. 3. The particle sizes of the DS, CPs, and RA were in the ranges of 0–0.30 mm, 0.30–4.75 mm, and 4.75–9.50 mm, respectively. As is evident from Figs. 2 and 3, there are some crucial differences between solid waste aggregates and natural aggregates in concrete engineering. The DS had a more uniform gradation, with more than 90% of the grains smaller than 0.20 mm; this represented 'superfine' sand with a maximum grain diameter of 0.30 mm, i.e., much finer than river sand or machine-made-sand. As the intermediate particle size, the CPs are spherical, with more than 50% and 90% of the grains smaller than 2.3 and 4.0 mm, respectively. The shape of the RA particles is cuboid, and the maximum particle size of the aggregates should not be greater than 1/3 of the printing nozzle diameter to avoid blockage of the printing nozzle. The RA was obtained from a domestic recycling plant in China after the mechanical crushing, screening, and cleaning of the concrete. According to the Chinese national standard GB/T 25177-2010 'recycled coarse aggregate for concrete' [37,38], the 14-day expansion rate was less than 0.1%, indicating that there was little potential for alkali–silica reaction problems.

The measured physical properties included the bulk density, apparent density, and void fraction of the DS, river-sediment CPs, and RA. The various physical parameters of the DS, CPs, and RA are presented in Table 1.

From the measured results, the water absorption rate values ω_a of the RA and CPs reached 9.7% and 92.1%, respectively, after immersion in water for 24 h. The wrapping of old mortar on the surface of RA usually induces defects regarding a high water absorption and low density, which can be mitigated by using an oversaturated RA [39,40]. The honeycomb microporous structure inside ceramsite determines the high water absorption. Significantly, the ceramsite can absorb the free water in the fresh concrete material, greatly reducing the workability, and can also greatly increase the shrinkage of the material, although this latter effect can be mitigated by prewetting for 24 h [41]. The mechanical properties of concrete show a downward trend with an increase in ceramsite content [27]. Therefore, to avoid negative influences in this study, the RA and CP were initially blended with the additional water before the mixing of concrete to place them in the saturated and oversaturated surface states, respectively.

Table 1
Physical property index of aggregates.

Type	ρ_{ap} kg/m^3	ρ_{bu} kg/m^3	ν/%	ω_a (20 min)	ω_a (60 min)	ω_a (24 h)	Strength (MPa)
DS	2573	1405	45.39	/	/	/	/
CPs	1489	850	26.09	60	66.8	92.1	4.50
RA	3378	1788	47.07	5.6	5.8	9.7	9.70

2.2. Raw materials and mix proportion

The materials for 3D printing composite included:

- ordinary Portland cement (P.O 42.5), which provided a 28 d compressive strength of 48.6 MPa and flexural strength of 8.6 MPa;
- silica fume with a density of 1.6–1.7 g/cm^3 and specific surface area of 18–24 m^2/g;
- polycarboxylate superplasticiser with a solid content of 8% and water reducing rate of 27%; and
- a small amount (0.4%) of basalt fibre to improve the consistency and crack resistance.

To study the effects of particle grading on the performance of 3D printing concrete, mixture ratios were designed for CG, IG, and OG using interactions based on the theory of particle interference [42]; these mixes were represented by the terms Mix-CG, Mix-IG, and Mix-OG, respectively. The grading curves are shown in Fig. 3(a). The average

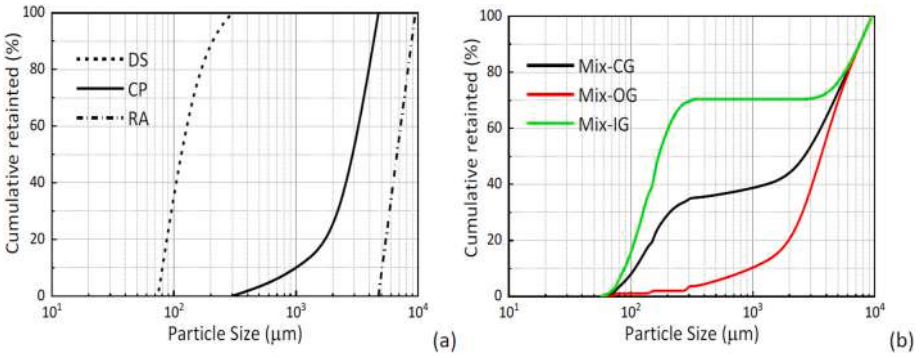

Fig. 3. (a) Particle size distribution and (b) gradation design curve of solid waste aggregate gradation.

particle size of the CPs was 3.8 mm, and approximately 70% of the particle sizes were distributed in 2.36–4.75 mm, indicating that particles with sizes between 0.3 and 2.36 mm were insufficient. The interrupted particle size range of the three raw particle materials made it difficult for the grading curve of Mix-CG to achieve excellent continuity. The raw materials and mix proportions are presented in Table 2. The water binder ratio of the three groups of materials was set as 0.5. The dosage of the water-reducing agent was slightly adjusted in the preparation process to meet the desired printability. In the manufacturing processes, all of the cementitious materials and various particles were added and premixed evenly. Then, all of the premixed water and water-reducing agents were added into the mixer and stirred for ten min to obtain the final composites.

2.3. 3D printing equipment

A gantry-type 3D printer with maximum effective printing dimension of 1.8 m (L) × 1.8 m (W) × 1.5 m(H) was adopted. The extrusion system adopted a screw rotation extrusion mode, which can realise the uniform and stable extrusion of materials. The opening diameter of the round nozzle was determined as 30 mm, to facilitate the extrusion of the aggregates. The prepared materials were pumped into the extrusion system, the horizontal printing speed was set as 50 mm/s, the vertical printing speed was set as 10 mm/s, the extrusion speed was set as 1.5 L/min, and the layer thickness was 10 mm.

2.4. Test methods

2.4.1. Assessment of flowability

The flowability was measured through a jumping table test, according to the Chinese national standard GB/T 50080–2016. Image acquisition was conducted during the test process to quantitatively characterise the fluidity of the prepared concrete. The sampling frequency was consistent with the jumping table frequency, as shown in Fig. 4(a). The flowability was characterised by two process parameters, i.e., the instantaneous flow velocity (v) and average flow velocity ($\bar{v}$), which were established in Eqs. (1) and (2), as follows:

$$v = \frac{l}{t} \tag{1}$$

In the above, v is the instantaneous flow rate (mm/s) of the mixtures at a certain time, l is the increase in the flow expansion diameter (mm) of the mixture after each vibration, and t is the unit time.

$$\bar{v} = \frac{L}{T} \tag{2}$$

Here, $\bar{v}$ is the average flow rate of the entire process (mm/s), L is the final flow expanding diameter (mm), and T is the time from de-moulding to flowing and resting.

2.4.2. Assessment of buildability

The buildability of the prepared mortar was assessed by loading the printed layers in compression at a specific loading rate to simulate the vertical layer-upon-layer stacking process, as shown in Fig. 4(b). The length of the test specimen was 300 mm, the width was 35 mm, and the height was 100 mm (printing of 10 layers). The compression loading rate was determined so as to be consistent with the actual printing speed of concrete materials, according to the following calculations. The self-weight of each layer of material was 3 N, the horizontal printing speed was 50 mm/s, and the elapsed time was 6 s. Therefore, the vertical loading rate was set as 0.5 N/s. The age at buildability testing was 30 min from the time when all of the water was added for mixing. The buildability was characterised based on the compressed deformation of the printed specimen during loading.

2.4.3. Assessment of physical property

The water absorption and density of the prepared 3D printing concrete were tested according to GB/T 50081-2019, 'Standard for test methods of physical and mechanical properties of concrete' [43]; specimens cut from a printed structure with a size of 100 mm × 100 mm × 100 mm cut were adopted.

2.4.4. Assessment of mechanical strength

The interfaces between adjacent layers are critical to the mechanical and durability performances of printed concrete. It was expected that the interlayer bonding could be improved using embedded aggregates. The interlayer bonding strength was assessed using a direct splitting tensile test. The size of the split tensile specimen was 50 mm (L) × 35 mm (W) × 60 mm (H). The test adopted a loading rate of 0.05 MPa/s, and the split tensile strength was calculated using Eq. (3), as follows:

$$f_{ts} = \frac{2F}{\pi A} \tag{3}$$

In the above, f_{ts} is the splitting tensile strength (MPa), F is the failure load (N), and A is the splitting area of the specimen (mm^2).

The printed samples were placed in a moist cabinet for proper curing at an ambient temperature of 20 ± 1 °C and relative humidity of 95 ± 5% for 28 days. After that, the splitting tensile strength test was conducted under a laboratory environment at a temperature of 23–25 °C and relative humidity of 30–65%.

2.4.5. Assessment of shrinkage property

Samples with dimensions of 300 mm (L) × 100 mm (H) × 35 mm (W) were printed for assessment of the shrinkage; the print speed was 50 mm/s, the squeezing speed was 1.5 L/min, and the layer thickness was 10 mm. A nozzle with a diameter of 30 mm was adopted. The early age shrinkage evolution within the first 24 h was tested by using a laser displacement meter for non-contact measurement. The data were collected hourly, in the setup shown in Fig. 5(a). After a testing period of 24 h, a dial gauge was set up on the printed samples for contact measurement, and the data collection frequency was daily for 28 d (in the setup shown in Fig. 5(b). The positions of the laser displacement meters and dial indicators on both sides of the printed specimen were controlled so as to be on the same straight line in the same horizontal plane. As above, the entire test process was conducted under the laboratory environment at a temperature of 23–25 °C and relative humidity of 30–65%.

2.4.6. Assessment of meso-structure by computed tomography (CT) scanning

Non-destructive X-ray CT scanning has been widely adopted to provide accurate identification of the meso/microscopic structures of engineering materials. In this study, advanced CT technology was employed to detect the voids and weak bonding interfaces formed by the filaments, distribution patterns, and skeletons of the various aggregates, as well as the relative positions between the fracture path and interfaces.

Table 2
Mix proportions for 3D printing composite by mass ratios.

Mixtures	OPC	SF	RA	CP	DS	Superplasticizer	Water	Basalt fiber
Mix-CG	0.8	0.2	0.63	0.78	0.69	0.017	0.5	0.4 vol %
Mix-IG			0.63	0	1.47	0.018		
Mix-OG			0.63	1.47	0	0.015		

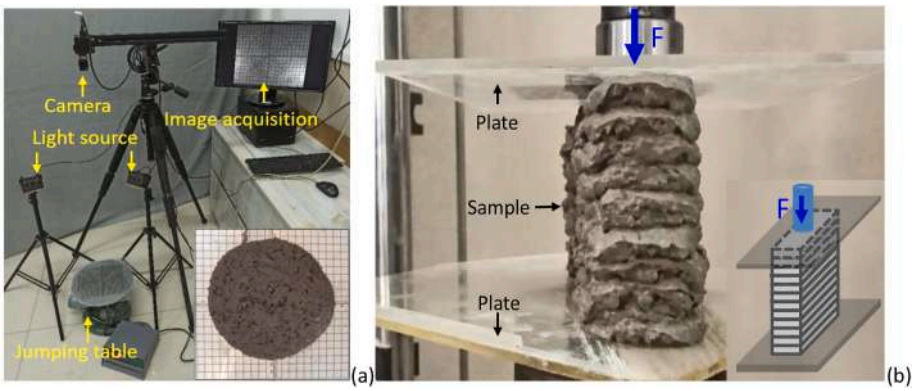

Fig. 4. (a) Jumping table test for measuring flowability, (b) compression test for measuring buildability.

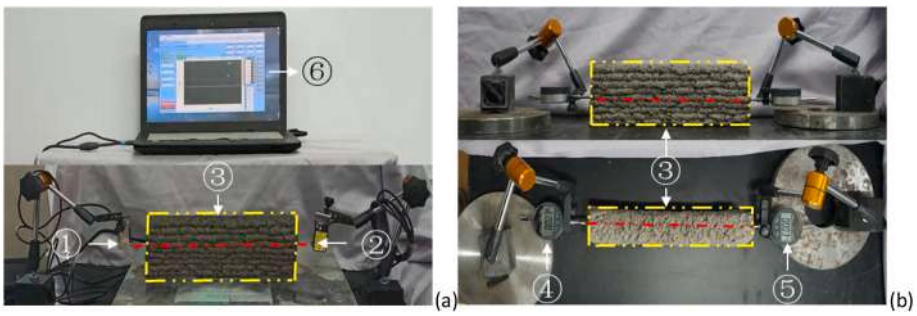

Fig. 5. (a) Non-contact shrinkage test (0–24 h), (b) contact shrinkage test (1 d–28 d) ①Laser displacement meter 1; ②Laser displacement meter 2; ③Printed sample; ④Dial gage 1; ⑤Dial gage 2; ⑥Displacement collector & data analysis.

For scanning, a high-resolution CT with a maximum spatial resolution of 10 μm was adopted, after rotating the sample 360° to improve the clearness of the detecting images; this satisfied the needs for reconstructing the meso-level structures.

3. Results and discussions

3.1. Effect of aggregate gradation on the flowability

The three types of mixtures, i.e. Mix-CG, Mix-IG, and Mix-OG, were tested for flowability and extrudability. Fig. 6 shows the jump tables test results. The rings with the same colour represent the spreading diameter at an identical time. The tests were repeated three times to obtain an average result. The final spreading diameters of Mix-CG, Mix-IG, and Mix-OG are 163 mm, 210 mm, and 178 mm, respectively. Both the particle grading and slurry layer produce distinct influences on the flowability of the concrete. Mix-CG shows the lowest flowability, demonstrating the effect of a skeleton formed by the continuous grading of particles, which can restrict the spreading flow of the composites. According to the results from Zhang et al. [33], the excess slurry layer acts as the lubrication layer between sand particles. The reduction of the excess slurry layer thickness will lead to an increase in the yield stress of the mortar. Due to the lack of desert sand, the specific surface area of Mix-OG is less than Mix-CG, the rich slurry thickness increases, and therefore the flowability is greater than Mix-CG. The aggregate of Mix-IG is composed of recycled aggregate and desert sand, and the particle size difference between them is large. The interlocking is ineffective and the inhibition effect on the fluidity of the composite is insignificant, therefore the largest flowability is performed.

The measured instantaneous flow rate and average flow rate are shown in Fig. 7. For Mix-CG, the skeleton effect between aggregates is evident, owing to the existence of the various particle sizes. The instantaneous flow velocity curve shows a gradual and slow downward trend during the flow process owing to aggregate friction and mechanical interlocking, as depicted in Fig. 7(a). Mix-IG lacks an intermediate particle size, the recycled coarse aggregates are in a suspended state in the freshly mixed material, and the skeleton effect is not apparent. The flow behaviours at the early stages are closer to the characteristics of mortar. As the material flows and the recycled coarse aggregate gradually makes contact, the skeleton effect appears, and the flow speed decreases. Therefore, the instantaneous flow velocity curve initially declines, and becomes slow. Mix-OG lacks small-grain aggregates and is rich in medium- and large-grain aggregates. The skeleton effect is evident, owing to the close contact and interlocking of the aggregates in the early flow stage, and the flow velocity is smaller than Mix-IG. With the flow and spreading process, the RAs and CPs separate, and the interlocking effect is relieved with an increase in the flow rate. At the later stages of flowing, the coarse materials in contact with each other become a major factor in the skeleton and further reduce the flow velocity, so that the instantaneous flow curve is high in the middle, and low at both ends.

The average flow speed is obtained by measuring the cumulative flow diameter at a specific point in time, as shown in Fig. 7(b). The total flow is substantially linear with time, with the slope of the line representing the flow velocity. The average flow rates of Mix-CG, Mix-IG, and Mix-OG are 2.36 mm/s, 3.52 mm/s, and 2.64 mm/s, respectively. The average flow speed reflects the overall influence of the aggregate skeleton on the concrete workability. The smaller the value of the speed, the more the material is affected by the aggregate skeleton. As a result, the skeleton effect of Mix-CG is the most evident, followed by those of Mix-OG and Mix-IG. Mix-IG has the weakest aggregate skeleton.

A printing material containing coarse aggregate with a spreading diameter of 163 mm (Mix-CG) can still be smoothly extruded. This is similar to the case with 3D printing mortars [13], demonstrating that the addition of the aggregate hinders the fluidity of the material but does not reduce its extrudability, based on the premise that the particle size of the

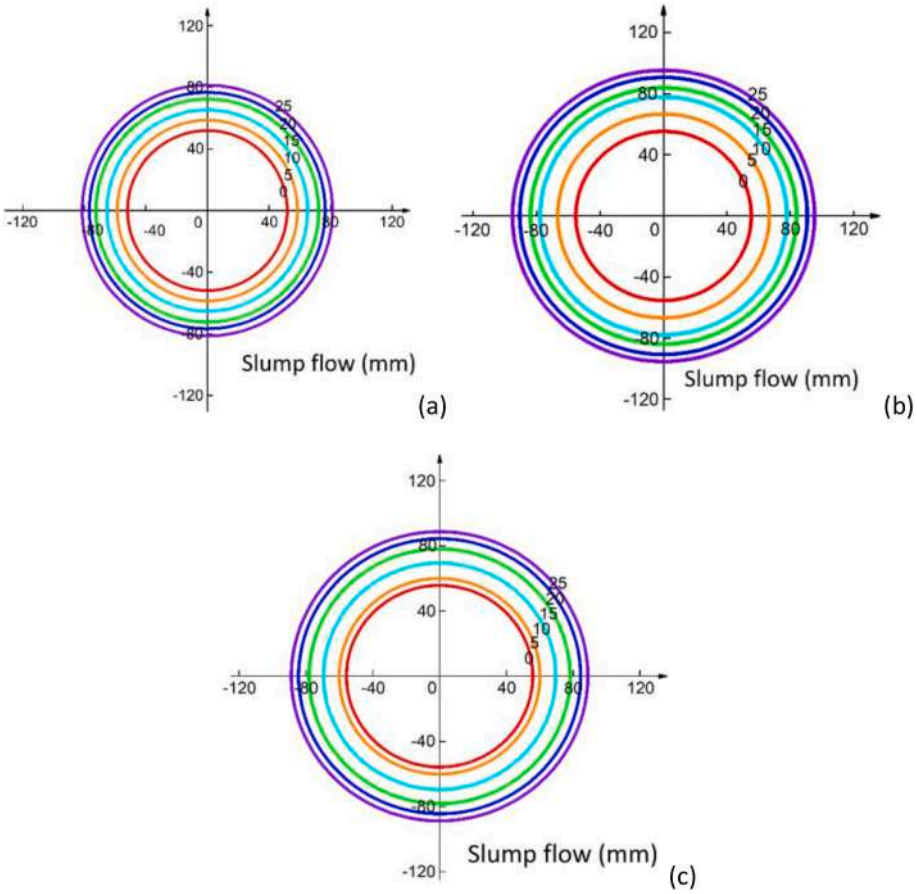

Fig. 6. Flowability evaluation of (a) Mix-CG, (b) Mix-IG, and (c) Mix-OG, based on measuring the spreading diameter.

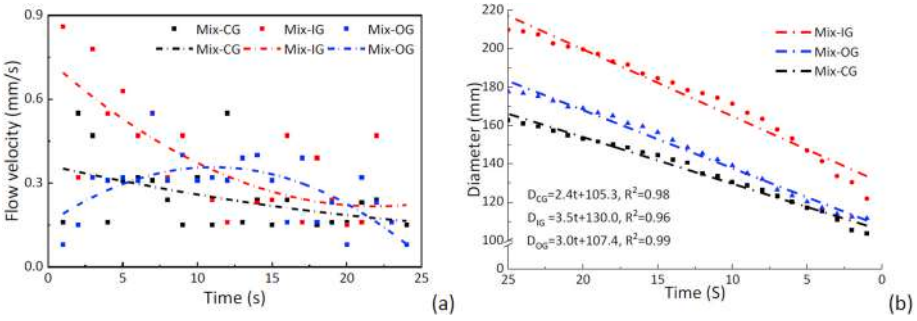

Fig. 7. (a) Instantaneous flow rate, (b) average flow velocity of various mixtures.

maximum aggregate particle is smaller than the nozzle size.

3.2. *Effect of aggregate gradation on the buildability*

The failure of the buildability has three modes: collapsing failures, shear failures, and buckling failures [44–47]. The stability issues related to a collapsing failure can be avoided by optimising the early stiffness of the material with accurate control of the printing setting, and then performing a stable layer stacking process. In this section, the evaluation and prediction of the buildability is mainly focused on the shear failure of the material at the early printing stage, i.e. before the initial setting.

Fig. 8 shows the deformation curves of different grading materials in the early stages after exposure to continuous compression. A mortar material lacking RA and ceramsite (denoted as 'no coarse aggregate' (NCA)) was tested for comparison. It can be seen from the test results that the gradation composition of the aggregate has a more significant impact on the buildability of the printable material. As shown in Fig. 8 (a), the deformation of the NCA gradually increases with the vertical pressure, and the material fails when reaching the peak load, showing an apparent yield failure limit. The peak load is 18 N and corresponds to a compression deformation of 3 mm, equivalent to the self-weight of continually stacking six layers with a thickness of 10 mm if no extrusion pressure is applied. Extrusion pressure is additionally produced due to the nozzle standoff distance is set as smaller than the nozzle diameter [48]. Therefore, the actual layers that can be sustained is smaller than the predicted one. The destruction states from the test results show that a shearing cracking occurs at the 6th layer position, as shown in Fig. 9(a).

The ultimate yielding load of Mix-CG is 91 N, and the deformation at peak compression is 25 mm, corresponding to a compressive strain of 2.5%. The yield stress is equivalent to the self-weight of continually stacking 30 layers if no extrusion pressure is applied. As the loading continues, the curve gradually rises again after a brief drop, as shown in

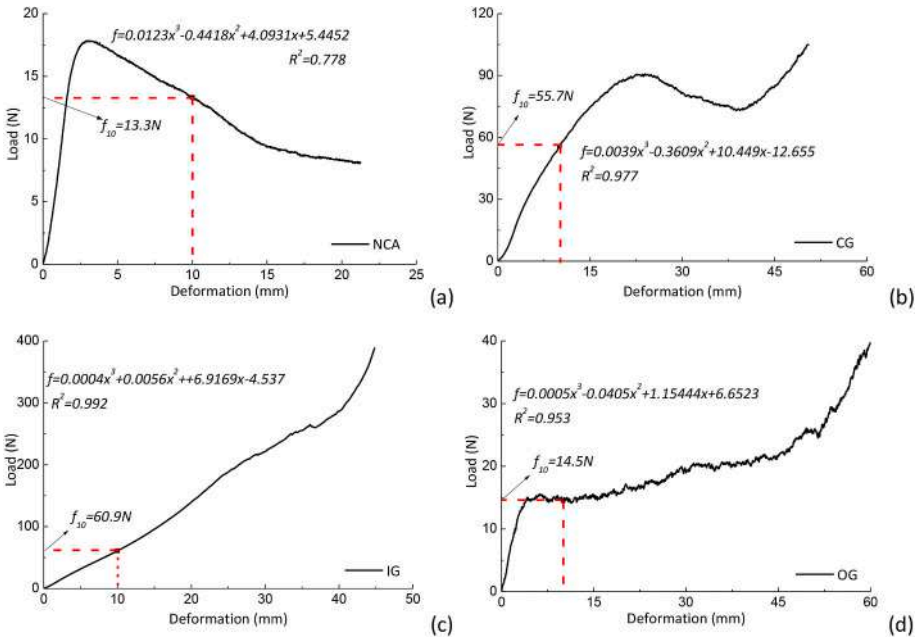

Fig. 8. Constructive load-displacement test curves of (a) NCA, (b) Mix-CG, (c) Mix-IG, (d) Mix-OG.

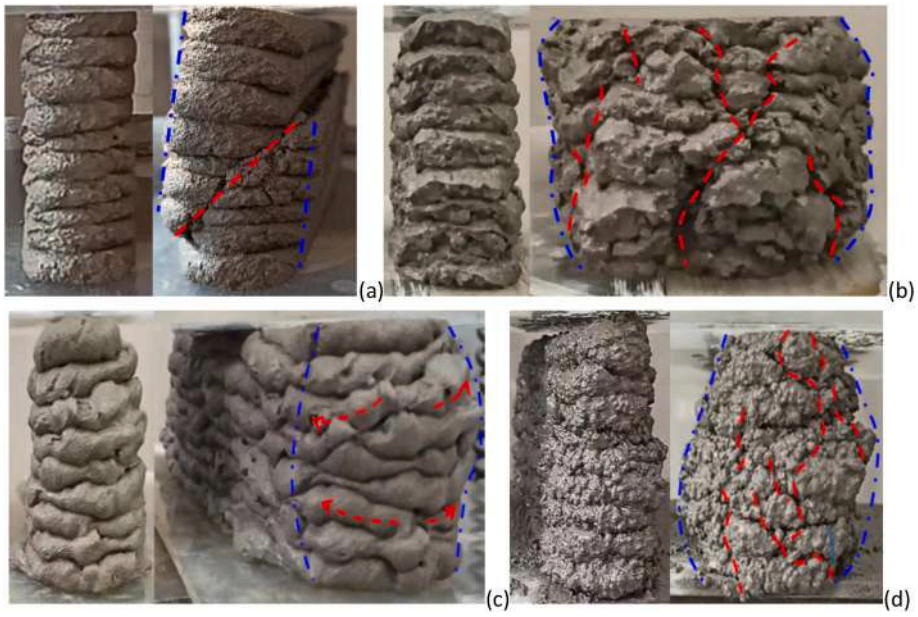

Fig. 9. Test destruction (a) NCA, (b) Mix-CG, (c) Mix-IG, (d) Mix-OG.

Fig. 8(b). This may be because the initial states of the stacked materials and internal cementitious structure are destroyed at the peak stage. The internal aggregates are squeezed and misaligned, and the vertical and lateral deformations continue to increase under compressive loading. The three-dimensional skeleton network formed by the particles is compacted, and the particles contact each other and can continue to bear the external load; thus, the curve rises again. However, because of their low degree of hydration at an early age, the cementitious materials provide low cementation and cohesion; when large deformations are produced, cracks form and propagate through the particle boundaries, resulting in separation from each other, as shown in Fig. 9(b).

The vertical deformation of Mix-IG increases gradually with the external load, and there is no evident ultimate failure load, as shown in Fig. 8(c). With the gradual increase in the bearing capacity, the lateral deformation increases. Mix-IG lacks medium-sized particles, large particles are suspended in the mortar, and the skeleton effect is weak. The effective stress mainly arises from the cohesion of the mortar. Under a compression load, the large particle aggregate moves and settles. The aggregate does not show a bearing performance owing to the particle separation, so the deformation increases gradually. However, when the vertical deformation value is greater than 40 mm, the vertical compression deformation exceeds 40%, and the bearing capacity increases rapidly. It can be inferred that under the action of an external force, the large particle aggregates contact and occlude each other owing to continuous movement and play a certain role in skeleton support for bearing the external load. However, owing to the large vertical and horizontal deformation, as shown in Fig. 9(c), Mix-IG cannot meet the volume stability requirements for printing.

In Mix-OG, the vertical deformation also increases with the load. When the load is 15 N, Mix-OG is compressed 4.5 mm (compression deformation rate 4.5%), and the strain rate rapidly increases. The displacement reaches 50 mm (compression deformation rate is 50%), the bearing capacity is enhanced and the load curve rises again, as shown in Fig. 8(d). At the inflexion point with a load of 15 N, the initial cementitious structure of the printing material is destroyed, as shown in Fig. 9(d). As the loading continues, the larger dosage CPs containing spherical shapes begin to move (e.g., rolling), resulting in a rapid increase in the amount of deformation when the compression deformation rate is 50%. The RA with CPs of large particles are in dense contact, thereby forming a stable three-dimensional support grid again for bearing the load and deformation. However, in this case, there is a large separation between the aggregates, and thus the mixture cannot meet the demands for printing stability.

Comparing the buildable load–displacement curves of mixtures with different gradation compositions, the displacements of Mix-CG, Mix-IG, and Mix-OG are 2.7 mm, 2.4 mm, and 4.1 mm, respectively, when 15 N is taken, i.e., immediately before the NCA reaches its peak bearing capacity. When the compression amount is 5 mm, i.e., the first inflexion point of the curve of Mix-OG, the loads of Mix-CG, Mix-IG, and Mix-OG are 31.5 N, 31.8 N, and 14.7 N, respectively. In this deformation situation, the NCA has been destroyed. At this stage, the compression deformation is relatively small, and the embedded aggregate system does not exhibit evident movement and settlement. It can be seen from the data that Mix-CG and Mix-IG have the same resistance to deformation, which is far better than that of Mix-OG. The bearing capacity of Mix-CG and Mix-IG is approximately two times higher than that of Mix-OG under the condition of a 5% compression deformation. The results demonstrate that the skeleton effect of the aggregate has an evident effect on improving the buildability of materials; Mix-OG has the largest compression under the same load, indicating that the ball effect of the ceramsite ball weakens the constructability of materials, and is not conducive to stable stacking.

Further analysis of the construction load–displacement curves of the different materials reveals that the materials have a high bearing capacity and small deformation at the initial stage of the constructive bearing capacity, which is a construction area that satisfies the buildability. After the ultimate bearing capacity is exceeded, the mid-term bearing capacity is reached. At this time, the load-bearing capacity has a small change range and a large deformation amplitude, and the built structure is gradually destroyed in a material failure zone. In the later loading stages, the internal particle sizes of the materials are compact, and the load-bearing capacity increases rapidly. The full curve of the constructive load-bearing characteristic of the printable material is S-shaped.

Fig. 10 shows the 3D reconstruction structure for each 3D printing mixture based on CT scanning, which can directly display the spatial distribution of the aggregates in printing materials. The aggregate is evenly distributed in the specimens, without interlayer spacing. Although there is no vibration process in the traditional casting process, the layer-by-layer stacking process is also conducive to achieving a uniform distribution of aggregates. The framework formed by overlapping aggregates has higher early stiffness, and the ability of the material to bear the self-weight load of the subsequently stacked material is improved. Therefore, the effect of the aggregate skeleton can significantly enhance the buildability of printing materials.

For printing materials at the same age, the stacking bearing capacity depends on the skeleton support system formed by the aggregates, and on the cementation and cohesion provided by the mortar materials. The construction process model for freshly mixed concrete materials can be explained to a certain extent by referring to the effective stress principle in soil mechanics [45,49].

Fresh concrete material is a saturated fresh material composed of a pore fluid formed by free water and pore gas, cementitious materials, and an aggregate skeleton. The total stress is shared by the three, as shown in Fig. 11. The effective stress σ' overcomes the relative slip rolling and other deformations between the particles and is the early

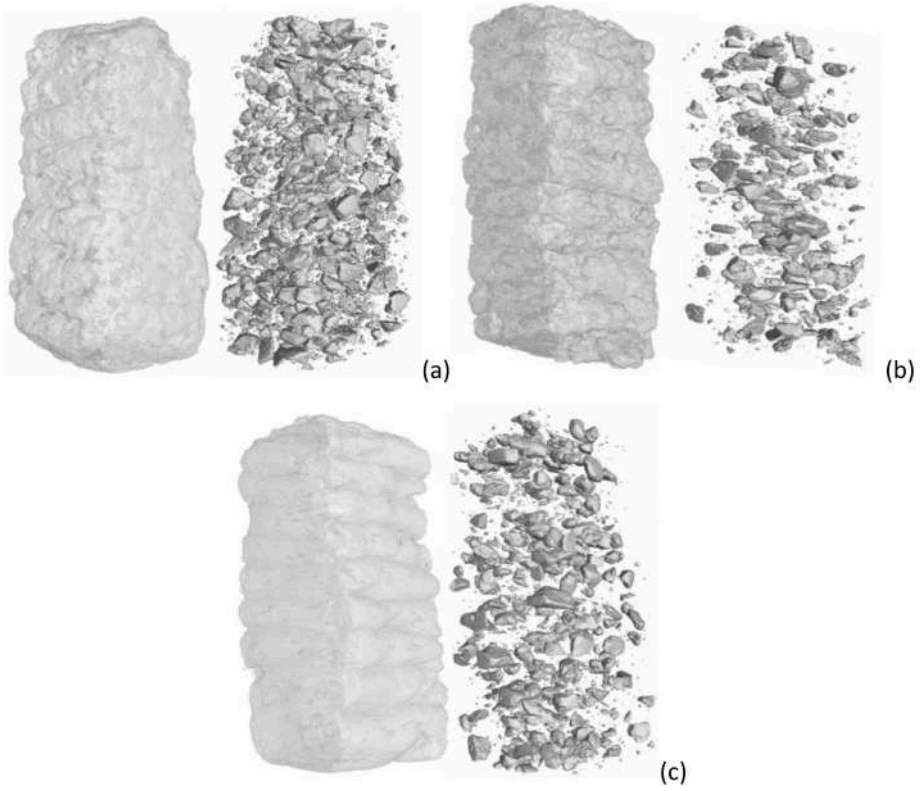

Fig. 10. Visualisation of 3D reconstruction meso-structures of (a) Mix-CG, (b) Mix-IG, and (C) Mix-OG.

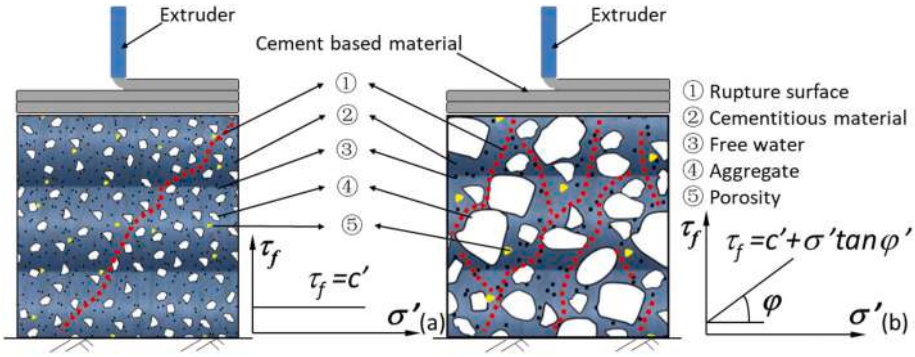

Fig. 11. Schematic diagram of shear resistance of fresh concrete materials (a)without coarse aggregate (b) with coarse aggregate.

origin of the bearing capacity. The pore fluid only makes the cementitious materials and aggregates subject to isotropic pressure and cannot provide shear resistance.

Therefore, the deformation and strength of the materials depend only on the effective stress. The total stress (σ) on any plane in the material can be divided into two parts: the effective stress (σ') provided by cementitious materials and aggregate skeleton, and the pore pressure (u) provided by the pore fluid, shown in Eq. (4) as follows:

$$\sigma = \sigma' + u \tag{4}$$

From evaluating the bearing characteristics of composite materials with different coarse aggregate particle compositions, it can be seen that the aggregate gradation determines the internal friction angle ϕ', and further determines the shear resistance of fresh materials under the same cohesion. The 3D printing material with NCA excludes coarse aggregates, fine particles are suspended in the cementitious system, the shear strength of the material is mainly provided by the cohesion of the cementitious material, and the shear failure is an inclined plane failure, as shown in Fig. 11(a). The friction and mechanical interlocking forces between the aggregates increase the shear resistance of the materials when larger particles are added. The shear resistance of Mix-CG, Mix-IG, and Mix-OG is provided by both the cohesion of the cementitious materials and the friction and bite force of the aggregates. The shear failure basically presents multi-crack failure, as shown in Fig. 11(b).

Fig. 12 shows a comparison between the design print heights and actual print heights of the different mixtures under axial loading. Favourable buildability depends on the yield stress of the material, which is distinctly related to the gradations [44,50]. When the maximum design height is at a low value (taking five layers as an example, the corresponding design height-to-width ratio is 1.43), the aggregate characteristics and gradation have no evident influence on the buildability, as the self-weight stress generated by the superimposed materials on the upper layers does not reach the yield limit of the material.

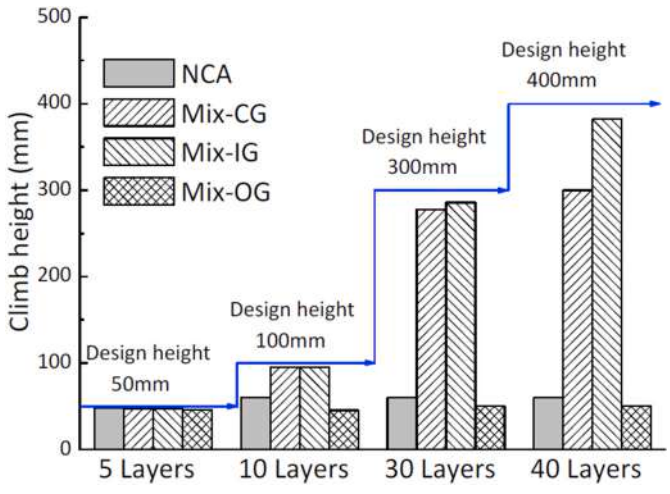

Fig. 12. Comparison of design height and actual printed height.

When the maximum design height reaches 10 layers, the actual print heights of the NCA and Mix-OG deviate significantly from the design height by 40% and 50%, respectively, i.e., a much higher level than those of Mix-CG and Mix-IG (where the design deviation of both is less than 5%). This shows that the contact, interlocking, and skeleton support between the aggregate particles can significantly improve the yield stress and enhance the constructability. However, there are many spherical ceramic particles (70% of the aggregate in Mix-OG). The ball effect of the ceramic particles greatly reduces the contribution of the coarse aggregate and cementitious material cohesion to the yield stress, making Mix-OG yield more easily than the NCA.

With a further increase in the design height, e.g., when the maximum design height is 40 layers, the corresponding design height-width ratio is 11.43, and the print deviations of Mix-CG and Mix-IG are 25% and 5%, respectively. The reason for this difference is that there are no ceramic particles in Mix-IG, whereas the ceramic sand in Mix-CG accounts for 37% of the aggregate. This further indicates that the ball effect of the ceramic particles weakens the contribution of the aggregate to the increase in the yield stress.

In other words, the skeleton interlocking of coarse aggregates can significantly increase the yield stress of the material. However, the ball effect of the ceramic particles reduces and replaces the occlusive effect of the aggregate, becoming the main factor affecting the construction quality; that is, with the increase in the ceramic content, the constructability decreases.

3.3. *Influence of aggregate grading on splitting performance*

In this section, a splitting test is applied to evaluate the influences of the aggregates on the mechanical properties of printing concrete, and particularly, to validate the influence of the embedded aggregates on the interlayer bonding properties. Fig. 13 shows the splitting test results for the various prepared materials. Owing to the inherent laminated mesostructure, the 3D printing materials show mechanical anisotropic properties, with insignificant differences. This may be owing to the combined effect of the spatial distribution characteristics of the aggregate and the weak surfaces between layers. For the casted materials, the strength of Mix-OG is the lowest, and may be affected by the high content of ceramsite particles. The porous structure makes it of low-strength, and easy to crack. The higher the ceramic content, the lower the strength of the material. For printing materials, the splitting test along the z-direction can more directly explain the influence of the aggregate on the interlayer properties. The interlayer tensile strength of Mix-OG is the highest, at 2.60 MPa, which is 41.2% and 52.7% higher than those of Mix-IG and Mix-CG, respectively. Meanwhile, the interlayer tensile strength of Mix-OG accounts for 92.9% of the

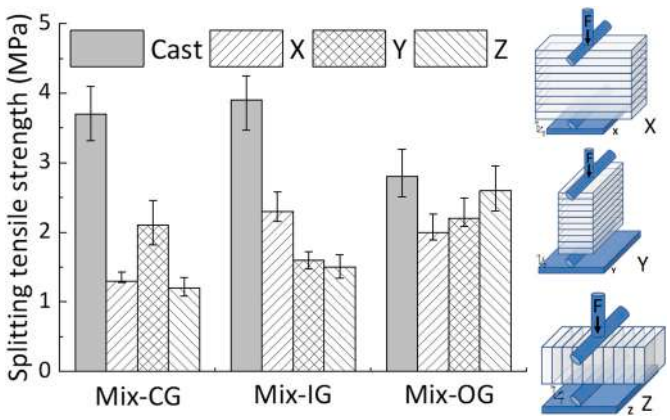

Fig. 13. Splitting tensile strength test results.

corresponding casted material, i.e., much higher than that of the other two materials. In the hardening stage of the composites, the saturated ceramic sand migrates its own water into the matrix to supplement water for the hydration reaction of the material, performing internal curing effect and contribute to the mechanical properties. In general, Mix-CG has the lowest splitting strength, whereas Mix-OG has a higher splitting strength, which is opposite to the case with the casted material.

Fig. 14 below shows the fracture morphology of the specimen along the Z direction. It is evident that the cross-section of Mix-CG is relatively flat, the angular RA is separated from the matrix of the cementitious material, and the damage occurs in the interface transition zone of the aggregate. Mix-OG produces the largest section roughness, and the protruding RAs observed at the interface are mostly wrapped with the cementitious matrix, indicating a good bonding performance of aggregate with matrix. The coarse RA can cross the weak surface between layers and plays a bridging role to help improve the weak surface between layers. Simultaneously, it is found that almost all of the ceramic particles are destroyed in the splitting process. From the fracture surface morphology, it can be seen that the printing interlayer interfaces of Mix-OG and Mix-IG have no significant effect on the fracture extension, whereas the straight fracture surface of Mix-CG basically coincides with the interlayer weak surface, indicating that the crack propagates along the printing interface. This is consistent with the test results for Mix-CG samples with lower splitting tensile strength.

In 3D printing concrete, the interlayer bonding performance determines the mechanical properties and durability of the printing structure. The interlayer tensile/shear capacity of the printing materials mainly depends on the bonding area between layers, skeleton effect formed by the interactions between aggregates, and strength of the aggregate itself.

Based on the above analysis, it is found that (1) recycled coarse aggregate can connect adjacent printing layers, improve the mechanical interlocking ability between printing layers, and enhance the bonding force between layers; this is validated and visualised by micro-CT tests on fracture sections (Fig. 14(d-f)). However, the improvement of the weak surface using RA also depends on the bond performance of the interface transition zone of the aggregate. The better the strength of the interface transition zone, the more favourable the aggregate is for improving the interlayer weak surface. (2) The splitting tensile strength of the cast material is weakened owing to the inherently low strength of ceramsite particles, but the interface strength is improved. This may be owing to the pre-soaking process before blending into the concrete. In the printing process, the interfaces are inevitably exposed to air, which can easily accelerate the evaporation of water; accordingly, stacking without vibration can easily cause small gaps/voids at the interfaces. These factors weaken the bonding performances between the layers. A ceramic aggregate treated by soaking water can provide moisture for the hydration of the interlayer materials, and the internal curing of the ceramic particles enhances the hydration degree and formation of hydration products, thereby improving the interface bonding strength. Meanwhile, the moisture stored in the porous structure of the ceramic particles can also improve the microstructure of the interface transition zone of the RA and improve the wrapping ability of aggregate and cementitious matrix, as shown by the fracture surface morphology depicted in Fig. 14(c).

3.4. Effect of three aggregate gradation on the shrinkage property

3D printing materials are easily prone to producing micro shrinkage cracks, owing to a lack of aggregate and/or the high proportion of cementitious materials. The proper addition of coarse aggregate is an effective solution for alleviating the shrinkage problems of 3D printing materials.

Fig. 15 and Fig. 16 present the instantaneous and cumulative shrinkage of the prepared materials as the surrounding temperature and relative humidity change in the early and curing periods. From the early period shrinkage results with non-contact measurement given in Figs. 15 (a) and Fig. 16(a), it can be seen that the cumulative shrinkages of Mix-CG, Mix-IG and Mix-OG are 1022 μm/m, 698 μm/m, and 607 μm/m, respectively, accounting for 84.1%, 93.1%, and 90.0% of the entire day

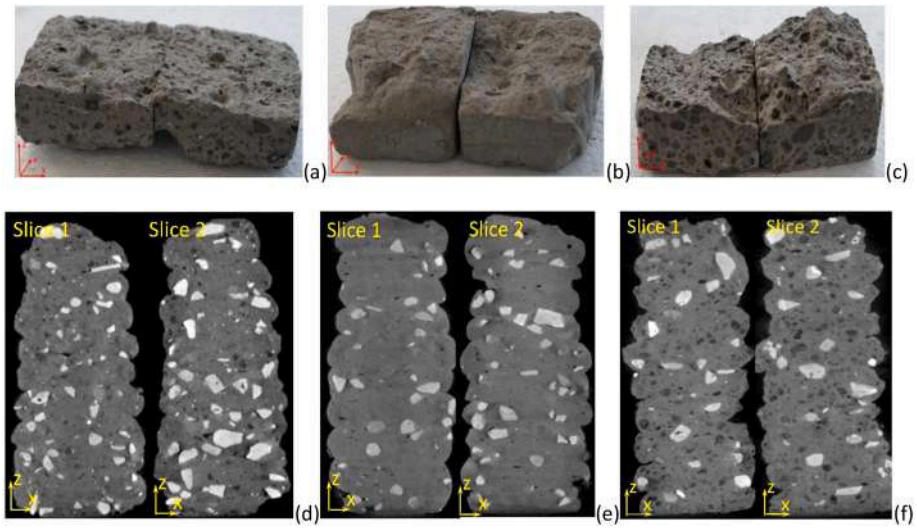

Fig. 14. Fracture morphologies of (a) Mix-CG, (b) Mix-IG, and (c) Mix-OG, and micro-CT scanning slices of (d) Mix CG, (e) Mix-IG, and (f) Mix-OG.

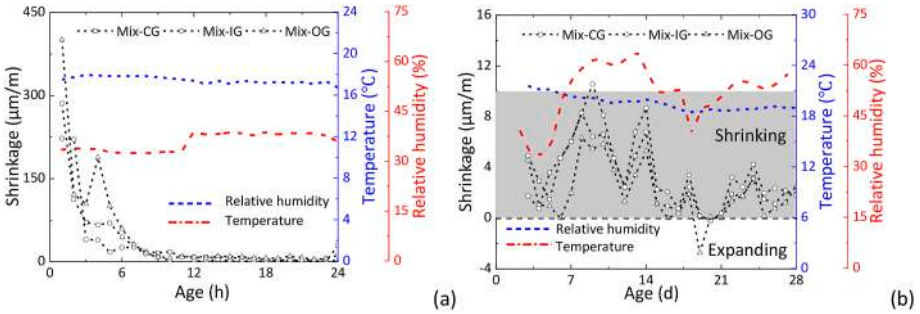

Fig. 15. Shrinkage measurement of materials at (a) early age (0–24 h) and (b) curing period (1–28 d).

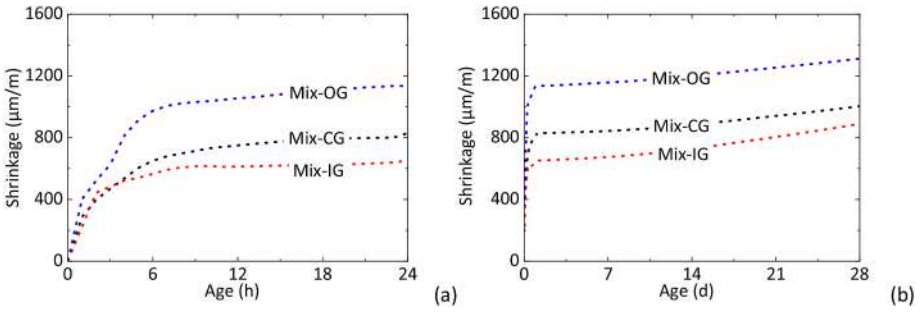

Fig. 16. Cumulative shrinkage test results (a) early age and (b) curing period.

(0–24 h, 1135 μm/m, 829 μm/m, and 652 μm/m), respectively. The shrinkage is mainly within the first 8 h at an early age (0–24 h), tends to slow after 8 h, and stabilises within 10 μm/m, i.e. similar results to those in Ref. [40].

The shrinkage results from contact measurements show that the shrinkage changes with age. Fig. 16(b) presents the cumulative test results from the curing period. Mix-OG exhibits the maximum shrinkage at 1321 μm/m, followed by Mix-CG (1014 μm/m); the minimum shrinkage is shown by Mix-IG (903 μm/m). During the hardening period, the significant shrinkage is mainly concentrated on the first day. The 1-d shrinkages of Mix-CG, Mix-IG, and Mix-OG account for 81.8%, 72.2%, and 86.0% of the 28-d value, respectively. The shrinkage ratio from large to small is Mix-IG, Mix-CG, and Mix-OG under identical temperature and humidity environments, demonstrating the inhibitory effect of the aggregate on the later shrinkage of the material; it may also indicate the effectiveness of the pre-treatment of ceramsite on relieving shrinkage after hardening [21,41].

The shrinkage cracking of concrete materials mainly occurs in the early stage, and the shrinkage within the first 24 h is mainly autogenous shrinkage. Autogenous shrinkage occurs over three different stages after concrete mixing, namely, during the liquid phase, skeleton formation, and hardening [51]. During the liquid phase, the internal material of the concrete is movable, and can quickly repair the defects caused by shrinkage. During the skeleton formation and hardening phase, the shrinkage resistance of concrete increases with a more rigid structure. However, if the shrinkage value is greater than the anti-shrinkage ability, irreversible damage will occur, and the greater the shrinkage value, the more serious the damage. For 3D printing concrete materials, the material shrinkage causes greater challenges. Because the fluidity and setting time are too small and short with ordinary concrete, there is no liquid stage to fill in the voids wing to shrinkage. Moreover, the early shrinkage is mainly concentrated at 0–8 h after mixing with water, indicating a very serious potential threat for 3D materials of concrete.

From the shrinkage test results, it is possible to determine the differences in the shrinkage properties of Mix-CG, Mix-IG, and Mix-OG. Mix-OG produce the largest early age shrinkage, followed by Mix-CG, and the smallest is Mix-IG. Regarding the CP content, Mix-OG is the highest (CPs accounts for 70.0% of the total aggregate mass) followed by Mix-CG (37.1%); Mix-IG does not contain CPs. A value of 1000 μm/m at 24 h has been proposed in the literature [52] to characterise the high risk of cracking of concrete at an early age. Only Mix-OG shows a 24-h shrinkage higher than this critical value. The water-saturated ceramic particle can perform internal curing effect and be benefit to mitigate the drying shrinkage due to the water supplement. While the effects of internal curing on the shrinkage are influenced by many factors, such as the content of light-weight aggregate, relative humidity of surrounding environment, curing time etc. As the presented results, the shrinkage of composites increases with the content of ceramic aggregates, showing adverse influences. If this phenomenon is caused by the low relative humidity in the early ages and high evaporation speed induced by the large exposed area of printed concrete requires further in-depth investigation and analysis.

4. Conclusion

In this study, 3D printing materials with different grades of underutilised or waste solid aggregates were investigated. The printability properties of the fresh concrete and hardened concrete properties were evaluated, including the extrudability, buildability, mechanical properties, and shrinkage. The following conclusions can be drawn.

- The optimal gradation was found to be continuous. However, this advantage was somewhat weakened by the CPs.
- The instantaneous flow velocity and average flow velocity were found to be adequate measures of the fluidity of 3D printing concrete materials with RA, CPs, and DS. Good fluidity was achieved when the average flow velocity and expanded diameter were in the ranges of 2.3–3.5 mm/s and 160–210 mm/s, respectively.
- Increasing compression loading was used to simulate the accumulated layer loading during the printing process. The findings indicated that the skeleton function of Mix-CG has an evident effect. This is confirmed by the failure mode, in which the aggregate is surrounded by cracks on the fracture surface. Mix-IG has a weak skeleton effect. This was confirmed by the failure mode, which was along

a 45° angle with the horizontal direction, i.e., similar to the failure mode without aggregates. Owing to the lubrication effect of CPs, Mix-OG showed a more evident fluidity failure under the same load relative to Mix-CG and Mix-IG.

- The existence of RA between the layers can roughen the interlayer interface, increasing the interlayer surface area. This results in an enhanced interlayer bond.
- Non-contact and contact shrinkage test methods with different gradations were used to evaluate the shrinkage properties. Both the 3D printing process and aggregate types adversely affect the shrinkage. The shrinkage performance requires further research.
- There are significant differences with or without large particle size aggregates in solid waste aggregates. The fluidity of the mix and type of printing equipment are the key parameters in determining whether a mix is printable.

Declaration of competing interest

The authors declare that they have no known competing financial interests or personal relationships that could have appeared to influence the work reported in this paper.

Acknowledgments

The authors would like to acknowledge the financial support by the National Natural Science Foundation of China (No. 51878241, No. 51808183, and No. 51627812), Hebei Science and Technology Department (18391203D) and Natural Science Foundation of Tianjin (No. 20JCYBJC00710).

References

[1] H. Van Damme, Concrete material science: past, present, and future innovations, Cement Concr. Res. 112 (2018) 5–24.
[2] R.A. Buswell, W.R. Leal de Silva, S.Z. Jones, J. Dirrenberger, 3D printing using concrete extrusion: a roadmap for research, Cement Concr. Res. 112 (2018) 37–49.
[3] J. Zhang, J. Wang, S. Dong, X. Yu, B. Han, A review of the current progress and application of 3D printed concrete, Compos. Appl. Sci. Manuf. 125 (2019) 105533.
[4] B. Furet, P. Poullain, S. Garnier, 3D printing for construction based on a complex wall of polymer-foam and concrete, Addit. Manuf. 28 (2019) 58–64.
[5] L. Wang, H. Jiang, Z. Li, G. Ma, Mechanical behaviors of 3D printed lightweight concrete structure with hollow section, Archiv. Civil Mech. Eng. 20 (1) (2020) 16.
[6] L. Wang, Z. Tian, G. Ma, M. Zhang, Interlayer bonding improvement of 3D printed concrete with polymer modified mortar: experiments and molecular dynamics studies, Cement Concr. Compos. 110 (2020) 103571.
[7] World's First 3D Printed Reinforced Concrete Bridge Opened, 2017. https://www.tue.nl/en/our-university/departments/built-environment/news/17-10-2017-worlds-first-3d-printed-reinforced-concrete-bridge-opened/.
[8] Guinness Certifies Prefabricated 3D-printed Zhaozhou Bridge, hebei university of technology, 2020. https://eweb.hebut.edu.cn/newsevents/hebutbulletin/98496.htm.
[9] The First Fabricated 3D Printing Bus Stop Appeared in Nanjing Jiangbei New Area, 2019. http://www.nanjingiam.com/cases.html?id=21.
[10] V. Mechtcherine, F.P. Bos, A. Perrot, W.R.L. da Silva, V.N. Nerella, S. Fataei, R.J. M. Wolfs, M. Sonebi, N. Roussel, Extrusion-based additive manufacturing with cement-based materials – production steps, processes, and their underlying physics: a review, Cement Concr. Res. 132 (2020) 106037.
[11] N. Roussel, H. Bessaies-Bey, S. Kawashima, D. Marchon, K. Vasilic, R. Wolfs, Recent advances on yield stress and elasticity of fresh cement-based materials, Cement Concr. Res. 124 (2019) 105798.
[12] Y. Wu, B. Lu, T. Bai, H. Wang, F. Du, Y. Zhang, L. Cai, C. Jiang, W. Wang, Geopolymer, green alkali activated cementitious material: synthesis, applications and challenges, Construct. Build. Mater. 224 (2019) 930–949.
[13] G. Ma, Z. Li, L. Wang, Printable properties of cementitious material containing copper tailings for extrusion based 3D printing, Construct. Build. Mater. 162 (2018) 613–627.
[14] T. Ding, J. Xiao, S. Zou, Y. Wang, Hardened properties of layered 3D printed concrete with recycled sand, Cement Concr. Compos. 113 (2020) 103724.
[15] J. Xiao, S. Zou, Y. Yu, Y. Wang, T. Ding, Y. Zhu, J. Yu, S. Li, Z. Duan, Y. Wu, L. Li, 3D recycled mortar printing: system development, process design, material properties and on-site printing, J. Build. Eng. 32 (2020) 101779.
[16] Y. Han, Z. Yang, T. Ding, J. Xiao, Environmental and economic assessment on 3D printed buildings with recycled concrete, J. Clean. Prod. 278 (2021) 123884.
[17] M.R.M. Saade, A. Yahia, B. Amor, How has LCA been applied to 3D printing? A systematic literature review and recommendations for future studies, J. Clean. Prod. 244 (2020) 118803.
[18] Y. Zhang, Y. Zhang, W. She, L. Yang, G. Liu, Y. Yang, Rheological and harden properties of the high-thixotropy 3D printing concrete, Construct. Build. Mater. 201 (2019) 278–285.
[19] S. De Carvalho Gomes, J.L. Zhou, W. Li, G. Long, Progress in manufacture and properties of construction materials incorporating water treatment sludge: a review, Resour. Conserv. Recycl. 145 (2019) 148–159.
[20] H. Sasanipour, F. Aslani, Durability properties evaluation of self-compacting concrete prepared with waste fine and coarse recycled concrete aggregates, Construct. Build. Mater. 236 (2020) 117540.
[21] X. Liu, T. Wu, Y. Liu, Stress-strain relationship for plain and fibre-reinforced lightweight aggregate concrete, Construct. Build. Mater. 225 (2019) 256–272.
[22] G. Mathews, R. Sinnan, M. Young, Evaluation of reclaimed municipal solid waste incinerator sands in concrete, J. Clean. Prod. 229 (2019) 838–849.
[23] Z. Tang, W. Li, G. Ke, J.L. Zhou, V.W.Y. Tam, Sulfate attack resistance of sustainable concrete incorporating various industrial solid wastes, J. Clean. Prod. 218 (2019) 810–822.
[24] J. Jiang, T. Feng, H. Chu, Y. Wu, F. Wang, W. Zhou, Z. Wang, Quasi-static and dynamic mechanical properties of eco-friendly ultra-high-performance concrete containing aeolian sand, Cement Concr. Compos. 97 (2019) 369–378.
[25] W. Yan, G. Wu, Z. Dong, Optimization of the mix proportion for desert sand concrete based on a statistical model, Construct. Build. Mater. 226 (2019) 469–482.
[26] S. Lopez-Querol, J. Arias-Trujillo, M. Gm-Elipe, A. Matias-Sanchez, B. Cantero, Improvement of the bearing capacity of confined and unconfined cement-stabilized aeolian sand, Construct. Build. Mater. 153 (2017) 374–384.
[27] J. Xie, J. Liu, F. Liu, J. Wang, P. Huang, Investigation of a new lightweight green concrete containing sludge ceramsite and recycled fine aggregates, J. Clean. Prod. 235 (2019) 1240–1254.
[28] J. Gong, W. Zeng, W. Zhang, Influence of shrinkage-reducing agent and polypropylene fiber on shrinkage of ceramsite concrete, Construct. Build. Mater. 159 (2018) 155–163.
[29] F. López Gayarre, J. Suárez González, R. Blanco Viñuela, C. López-Colina Pérez, M. A. Serrano López, Use of recycled mixed aggregates in floor blocks manufacturing, J. Clean. Prod. 167 (2017) 713–722.
[30] V. Revilla-Cuesta, M. Skaf, F. Faleschini, J.M. Manso, V. Ortega-López, Self-compacting concrete manufactured with recycled concrete aggregate: an overview, J. Clean. Prod. 262 (2020) 121362.
[31] S. Pranav, S. Aggarwal, E.-H. Yang, A. Kumar Sarkar, A. Pratap Singh, M. Lahoti, Alternative materials for wearing course of concrete pavements: a critical review, Construct. Build. Mater. 236 (2020) 117609.
[32] C. Maduabuchukwu Nwakaire, S. Poh Yap, C. Chuen Onn, C. Wah Yuen, H. Adebayo Ibrahim, Utilisation of recycled concrete aggregates for sustainable highway pavement applications; a review, Construct. Build. Mater. 235 (2020) 117444.
[33] C. Zhang, Z. Hou, C. Chen, Y. Zhang, V. Mechtcherine, Z. Sun, Design of 3D printable concrete based on the relationship between flowability of cement paste and optimum aggregate content, Cement Concr. Compos. 104 (2019) 103406.
[34] Y. Weng, M. Li, M.J. Tan, S. Qian, Design 3D printing cementitious materials via Fuller Thompson theory and Marson-Percy model, Construct. Build. Mater. 163 (2018) 600–610.
[35] G. Ma, Z. Li, L. Wang, F. Wang, J. Sanjayan, Mechanical anisotropy of aligned fiber reinforced composite for extrusion-based 3D printing, Construct. Build. Mater. 202 (2019) 770–783.
[36] G. Ma, Y. Li, L. Wang, J. Zhang, Z. Li, Real-time quantification of fresh and hardened mechanical property for 3D printing material by intellectualization with piezoelectric transducers, Construct. Build. Mater. 241 (2020) 117982.
[37] C.N. Standard, Recycled Coarse Aggregate for Concrete GB/T 25177-2010, 2010.
[38] C.N. Standard, Lightweight Aggregates and its Test Methods—Part 2 : Test Methods for Lightweight Aggregates GBT 17431.2-2010, 2010.
[39] R. Muduli, B.B. Mukharjee, Performance assessment of concrete incorporating recycled coarse aggregates and metakaolin: a systematic approach, Construct. Build. Mater. 233 (2020) 117223.
[40] A.Z. Bendimerad, E. Rozière, A. Loukili, Plastic shrinkage and cracking risk of recycled aggregates concrete, Construct. Build. Mater. 121 (2016) 733–745.
[41] T. Ji, D. Zheng, X. Chen, X. Lin, H. Wu, Effect of prewetting degree of ceramsite on the early-age autogenous shrinkage of lightweight aggregate concrete, Construct. Build. Mater. 98 (2015) 102–111.
[42] Y. Miao, S. Wang, L. Guo, J. Li, A method for quantifying the packing function of particles in packed aggregate blend, Construct. Build. Mater. 188 (2018) 607–614.
[43] C.N. Standard, Standard for Test Methods of Physical and Mechanical Properties of Concrete GB/T50081-2019, 2019.
[44] R.J.M. Wolfs, F.P. Bos, T.A.M. Salet, Early age mechanical behaviour of 3D printed concrete: numerical modelling and experimental testing, Cement Concr. Res. 106 (2018) 103–116.
[45] R.J.M. Wolfs, F.P. Bos, T.A.M. Salet, Triaxial compression testing on early age concrete for numerical analysis of 3D concrete printing, Cement Concr. Compos. 104 (2019) 103344.
[46] A.S.J. Suiker, Mechanical performance of wall structures in 3D printing processes: theory, design tools and experiments, Int. J. Mech. Sci. 137 (2018) 145–170.
[47] J. Kruger, S. Zeranka, G. van Zijl, 3D concrete printing: a lower bound analytical model for buildability performance quantification, Autom. Construct. 106 (2019) 102904.
[48] R. Comminal, W.R. Leal da Silva, T.J. Andersen, H. Stang, J. Spangenberg, Modelling of 3D concrete printing based on computational fluid dynamics, Cement Concr. Res. 138 (2020) 106256.

[49] R. Jayathilakage, P. Rajeev, J.G. Sanjayan, Yield stress criteria to assess the buildability of 3D concrete printing, Construct. Build. Mater. 240 (2020) 117989.
[50] R.J.M. Wolfs, F.P. Bos, T.A.M. Salet, Correlation between destructive compression tests and non-destructive ultrasonic measurements on early age 3D printed concrete, Construct. Build. Mater. 181 (2018) 447–454.
[51] Y.z. Zhuang, D.d. Zheng, Z. Ng, T. Ji, X.f. Chen, Effect of lightweight aggregate type on early-age autogenous shrinkage of concrete, Construct. Build. Mater. 120 (2016) 373–381.
[52] E. Holt, Contribution of mixture design to chemical and autogenous shrinkage of concrete at early ages, Cement Concr. Res. 35 (3) (2005) 464–472.